

# Characteristics of puffing activity revealed by ground-based, thermal infrared imaging: the example of Stromboli Volcano (Italy)

Damien Gaudin<sup>1,2</sup>  · Jacopo Taddeucci<sup>1</sup> · Piergiorgio Scarlato<sup>1</sup> · Andrew Harris<sup>3</sup> · Maxime Bombrun<sup>3</sup> · Elisabetta Del Bello<sup>1</sup> · Tullio Ricci<sup>1</sup>

Received: 4 May 2016 / Accepted: 14 February 2017 / Published online: 27 February 2017  
© Springer-Verlag Berlin Heidelberg 2017

**Abstract** Puffing, i.e., the frequent (1 s ca.) release of small (0.1–10 m<sup>3</sup>), over-pressurized pockets of magmatic gases, is a typical feature of open-conduit basaltic volcanoes worldwide. Despite its non-trivial contribution to the degassing budget of these volcanoes and its recognized role in volcano monitoring, detection and metering tools for puffing are still limited. Taking advantage of the recent developments in high-speed thermal infrared imaging, we developed a specific processing algorithm to detect the emission of individual puffs and measure their duration,

size, volume, and apparent temperature at the vent. As a test case, we applied our method at Stromboli Volcano (Italy), studying “snapshots” of 1 min collected in the years 2012, 2013, and 2014 at several vents. In all 3 years, puffing occurred simultaneously at three or more vents with variable features. At the scale of the single vent, a direct relationship links puff temperature and radius, suggesting that the apparent temperature is mostly a function of puff thickness, while the real gas temperature is constant for all puffs. Once released in the atmosphere, puffs dissipate in less than 20 m. On a broader scale, puffing activity is highly variable from vent to vent and year to year, with a link between average frequency, temperature, and volume from 136 puffs per minute, 600 K above ambient temperature, 0.1 m<sup>3</sup>, and the occasional ejection of pyroclasts to 20 puffs per minute, 3 K above ambient, 20 m<sup>3</sup>, and no pyroclasts. Frequent, small, hot puffs occur at random intervals, while as the frequency decreases and size increases, an increasingly longer minimum interval between puffs, up to 0.5 s, appears. These less frequent and smaller puffs also display a positive correlation between puff volume and the delay from the previous puff. Our results suggest an important role of shallow bubble coalescence in controlling puffing activity. The smaller and more frequent puffing at “hotter” vents is in agreement with the rapid rise of small gas pockets with only limited coalescence, while slower rise, allowing more time for coalescence, leads to larger but less frequent puffing at “colder” vents. This link between puffing style and vent thermal state points to a feedback between gas flux and magma temperature (and viscosity), where higher gas flux stirs and heats the magma, which, by getting less viscous, becomes a preferential way for bubble rise. Such a link has implications for the monitoring of the state of the shallow conduit at open-vent volcanoes as well as for determination of their total gas

Editorial responsibility: J. Dufek

**Electronic supplementary material** The online version of this article (doi:10.1007/s00445-017-1108-x) contains supplementary material, which is available to authorized users.

## Highlights

- An algorithm efficiently detects volcanic puffing from thermal high-speed videos.
- Six hundred seven puffs were studied to constrain their frequency, volume, and temperature.
- Smaller and more frequent puffing characterizes “hotter” vents.
- Puffing frequency at a vent reflects shallow bubble coalescence dynamics.
- The total volcano gas flux influences the number of simultaneously puffing vents.

✉ Damien Gaudin  
damgaudin@gmail.com

<sup>1</sup> Istituto Nazionale di Geofisica e Vulcanologia, Sezione Roma 1, Via di Vigna Murata, 605, Rome 00143, Italy

<sup>2</sup> Department of Earth and Environmental Sciences, Ludwig-Maximilians-Universität München (LMU), Theresienstr. 41, 80333 Munich, Germany

<sup>3</sup> Laboratoire Magmas et Volcans, Université Blaise Pascal, CNRS UMR 6524, IRDR 163 Clermont-Ferrand, France

budget, relevant for hazard forecast and environmental studies.

**Keywords** Puffing · Thermal infrared · Conduit conditions · Degassing · Strombolian activity · Stromboli

## Introduction

Strombolian activity is associated with low viscosity magmas, allowing the segregation of gas bubbles from the magma. The rise and the burst of large over-pressurized gas pockets at the surface of the magma column (Vergnolle and Jaupart 1986; James et al. 2008; Del Bello et al. 2012) generate mild, short-lived explosions, erupting a mixture of gas and pyroclasts to heights of tens to hundreds of meters (Barberi et al. 1993; Allard et al. 1994; Houghton et al. 2016) with inter-event durations of minutes to tens of minutes.

In addition to the abovementioned “normal Strombolian explosions,” the occurrence of puffing activity, i.e., the repeated emission of discrete gas volumes, has been reported, sometimes associated with a few incandescent bombs, with inter-event duration of a few seconds. After the first report at Stromboli (Ripepe and Gordeev 1999; Ripepe et al. 2002; Harris and Ripepe 2007), puffing has been recognized at an increasingly number of volcanoes worldwide, including Yasur (Vanuatu, Bani et al. 2013; Spina et al. 2015), Masaya (Nicaragua, Branan et al. 2008), and Villarica (Chile, Gurioli et al. 2008). From a remote sensing point of view, a puff has been defined by Harris and Ripepe (2007) as “the emission of air or steam in discrete packages so that the gas is emitted from the vent and/or rises in puffs (Sykes 1982)” while in other studies based on acoustics, a puff necessarily involves a significant overpressure (Ripepe et al. 1996; Landi et al. 2011). Following the first definition, in this paper, we chose to consider that overpressure is not a strict requirement to define puffing. Despite its frequent occurrence, puffing has been relatively poorly studied because the low gas release magnitude makes puffs difficult to detect. However, monitoring and interpretation of puffing activity is of twofold interest. First, the gas emitted during puffing represents a significant fraction of the degassing budget of the volcano (16–45% at Stromboli, according to Harris and Ripepe (2007); Tamburello et al. (2012)) and can help assess the degassing state of the magma (Oppenheimer et al. 2006; Burton et al. 2007). Secondly, the location and the intensity of puffing may be influenced by the shallow magma circulation system (Landi et al. 2011) and could be potentially used to anticipate hazardous changes in the explosive activity of the volcano (Ripepe et al. 2009).

Puffing was first characterized through infrasonic studies that provided constraints on the size and the pressure of the bursting bubbles (Ripepe and Gordeev 1999; Ripepe et al. 2002). However, the moderate temporal and spatial resolution

of these systems did not allow studying the finest features of the puffs, such as their precise locations and their individual time evolution after release. From a geochemical perspective, open-path Fourier transform infrared (OP-FTIR) spectroscopy (Burton et al. 2007) and ultraviolet spectroscopy (Tamburello et al. 2011, 2012) have given insights into the chemical composition and the origin of the gas. However, besides their limited sampling rate, such methods usually cannot be used unless there is light originating from a hot source or clear sky that then passes through the released gas, thus requiring a specific configuration of the study area and often preventing observations close to the vent (Branan et al. 2008).

Recently, thermal infrared has been used to detect the thermal signature of the hot gas released, allowing determination of the frequency and the radiant energy of the puffs. In most recent studies, the thermal infrared signal is measured in a large field of view above the vent, either using pyrometers (Johnson et al. 2004; Sahetapy-Engel et al. 2008; Bani et al. 2013) or by averaging the data from thermal infrared cameras (Harris and Ripepe 2007; Branan et al. 2008). The studied field of view includes the whole apparent surface of the puff. Thus, the amplitude of the measured signal depends not only on the puff temperature but also of its apparent surface area (Spampinato et al. 2011; Harris 2013). This “integrated temperature” is ideal for monitoring purposes but induces severe limitations for the description of the mechanisms of puff generation.

In this paper, we take advantage of a new generation of thermal infrared cameras for the study of puffing activity. The relatively high frame rate of the camera allows isolating and tracking individual puff events with a very short recurrence time, while the shape and the maximum apparent temperature of the puffs can be discriminated thanks to the high spatial resolution. We propose a new detection algorithm and use it to derive the main parameters of puffs—size, temperature, rise velocity, duration, and volume—as well as their evolution with time regardless of vent conditions. We use this algorithm to study eight snapshots of vent activity at Stromboli (Aeolian Islands, Italy) in order to (i) better understand the mechanisms and controls of puffing activity and (ii) assess the reliability of their monitoring via thermal infrared imaging.

## Data acquisition

Stromboli Island (Aeolian Islands, Italy) is a 926-m a.s.l. volcanic complex located in the Southern Tyrrhenian Sea, in a sector influenced by the opening of the Marsili oceanic basin and the migration of the Calabrian arc (Tibaldi et al. 2008). Stromboli is well known for its persistent explosive activity (Rosi et al. 2000), interrupted only by paroxysmal episodes occurring a few times per decade (Barberi et al. 1993). Since at

least 1776 (Washington 1917), the activity has been located on a terrace located 700 m a.s.l., hosting three main vent areas named according to their geographical position: South-West (SW), Central (C), and North-East (NE). Within these areas, vent location and activity is variable in the timescale of a few days to months (Harris and Ripepe 2007).

We collected high-speed thermal infrared videos during the three 1-week field campaigns (5–9 September 2012; 20–26 May 2013; 14–18 May 2014; see Table 1) during low to moderate seismic activity periods with, respectively, 13, 10, and 17 small intensity explosions per hour recorded by the seismic monitoring network (<http://www.ov.ingv.it/ov/en/monitoraggio-sismologico-di-stromboli/comunicati-giornalieri.html>); and low to medium-low amplitudes of VLP and tremor signals. For each of the 3 years of our field missions, puffing activity occurred at three (2012), four (2013), and seven (2014) individual vents distributed over all three vent areas (Fig. 1). However, a few days after the 2014 field campaign, an increase of the overall activity of the volcano occurred, followed by the emission of lava flows.

The geometry of the terrace and the location of the eruptive vents were different for each campaign. Accordingly, we hereafter label vent activities after their respective source vent and eruption year (e.g., NE14c marks the activity of the third (c) vent of the North-East vent area in 2014). Given that puffing activity at each vent varies on a timescale of minutes and puffing frequency is always higher than 0.2 Hz (see “Results”), we elected to illustrate each vent activity by using snapshots, consisting of one, representative, randomly chosen, consecutive minute of recording.

We used FLIR SC660 and SC655 uncooled thermal cameras, recording electromagnetic radiation in the 7.5–13- $\mu$ m waveband with a maximum definition of 640  $\times$  480 pixels at up to 30 and 200 frames per seconds, respectively. Camera location, depending on weather conditions, varied between 265 and 408 m away from the vents, with angles dipping between  $-1.3$  and  $-37.4^\circ$ . Depending on the lenses used, pixel resolution at the vent ranged

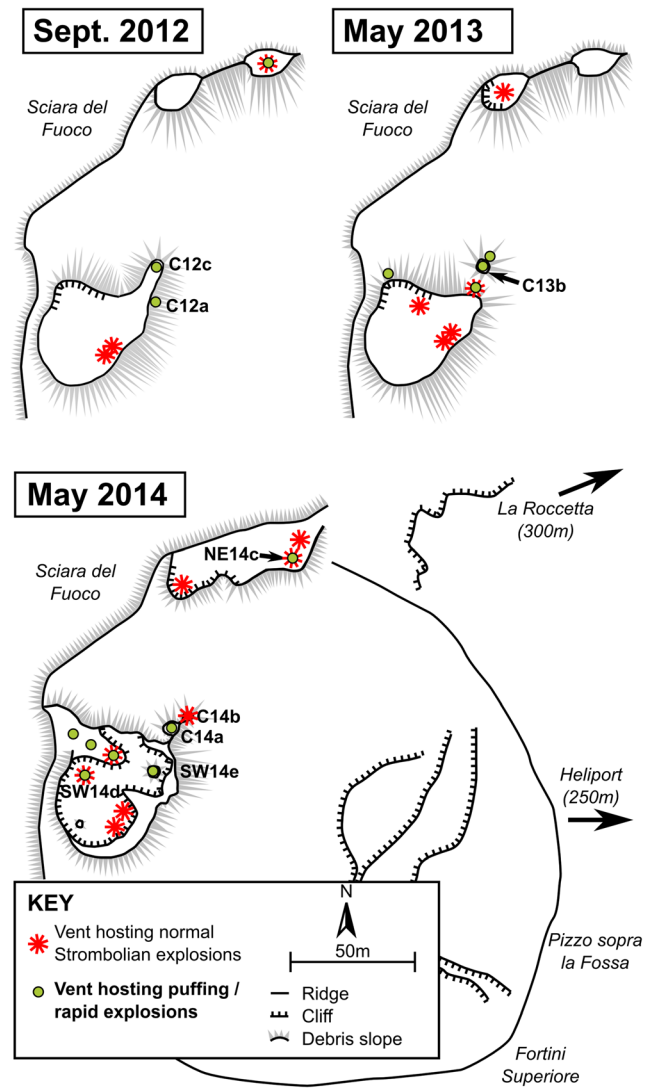


**Fig. 1** Location of the active vents during the three field campaigns. Only the labels of the vents presented in this study are reported

11.0–38.7 cm (see Table 1). Finally, the effects of the atmospheric absorption have been corrected in situ through the camera

**Table 1** List of the videos and recording parameters used in this study. All videos are 1-min long. The distances and slant angles are measured from the cameras to the vent, negative angles pointing downwards

Vent	Date and time of recording (GMT)	Location of the sensor	Slant distance	Dip angle ( $^\circ$ )	Camera	Pixel size	Frame rate	Number of analyzed puffs
SW14d	18/05/2014, 13:38	Pizzo	312 m	$-23.0$	FLIR SC655	12.9 cm	200 Hz	120
SW14e	18/05/2014, 12:15	Fortini Sup.	294 m	$-14.0$	FLIR SC660	37.9 cm	15 Hz	57
C12a	09/09/2012, 11:36	Pizzo	270 m	$-36.6$	FLIR SC655	11.2 cm	50 Hz	72
C12c	09/09/2012, 11:36	Pizzo	270 m	$-36.6$	FLIR SC655	11.2 cm	50 Hz	20
C13b	20/05/2013, 15:29	Pizzo	266 m	$-37.2$	FLIR SC655	11.0 cm	50 Hz	122
C14a	18/05/2014, 11:11	Pizzo	265 m	$-37.4$	FLIR SC655	11.0 cm	200 Hz	42
C14b	18/05/2014, 12:15	Fortini Sup.	300 m	$-13.7$	FLIR SC660	38.7 cm	15 Hz	136
NE14c	14/05/2014, 14:05	Rocchetta	408 m	$-1.3$	FLIR SC655	17.0 cm	50 Hz	38

software, relying on the humidity and the temperature of atmosphere and the distance vent/camera.

## Data processing

### The thermal infrared signal

Thermal infrared cameras are primarily designed to estimate the temperature of a solid surface by measuring the luminance  $L$ , i.e., the electromagnetic flux emerging from a specific solid angle (Spampinato et al. 2012; Harris 2013). In the ideal case of a blackbody,  $L$  is directly linked to the surface temperature through Planck's law (Planck 1901). Temperature computed from Planck's law is termed brightness temperature  $T_b$  (Harris 2013). In natural cases, part of the incoming electromagnetic signal may be reflected by the surface of the body or absorbed and backscattered by the atmosphere between the object and the sensor, so that  $T_b$  differs from the real surface temperature  $T$  (or kinetic temperature,  $T_k$ ). However, the effects of atmospheric absorption can be removed using dedicated software such as MODTRAN (Berk et al. 1987) or the commercial software of the cameras.

In the case of clouds and plumes, the origin of electromagnetic radiation recorded by the thermal camera  $L_{\text{cam}}$  is more complex. Indeed, if the cloud is thin enough, a fraction  $\tau$  of the electromagnetic signal may originate from the background, i.e., the volcanic rocks, the volcanic gas, and/or the atmosphere located behind the plume. Consequently,  $L_{\text{cam}}$  is (Chandrasekhar 1960; Cerminara et al. 2015):

$$L_{\text{cam}} = \tau L_{\text{bg}} + (1-\tau)L_p \quad (1)$$

$L_{\text{bg}}$  is the background luminance while  $L_p$  represents the electromagnetic signal that would have been emitted by the plume if it was opaque at the detected wavelength and can be used to estimate the average temperature of the plume. According to Beer-Lambert law, the transmittance of the gas plume is linked to its thickness and the concentration of the species in it (Verhoeven 1996; Cerminara et al. 2015)

$$\tau = \exp[-(\sum \gamma_i C_i)l] \quad (2)$$

where  $C_i$  is the volumetric concentration of the species  $i$ ,  $\gamma_i$  is the constant, species-specific absorption coefficient, and  $l$  is plume thickness in the direction of the beam. The transmissivity of the gas can be estimated using MODTRAN (Berk et al. 1987). For the range of compositions of magmatic gas of Stromboli (Burton et al. 2007), an undiluted (i.e., without entrained air) gas cloud 1 m across at atmospheric temperature would have an absorbance  $(1-\tau)$  ranging between 20 and 28% in the thermal infrared wavelengths (7.5–14  $\mu\text{m}$ ), i.e., about 100 times larger than that of the atmosphere (0.29%). Ash particles and water droplet would further increase puff

absorption. Thus, at first order, we can neglect the effect of atmosphere inside a puff and model the transmittance of a puff as follows:

$$\tau \approx \exp[-a l/d] \quad (3)$$

where  $d$  is the dilution of the plume and  $a$  a proportionality factor depending on the chemical composition and the solid particle contents of the puff.

### Video preprocessing

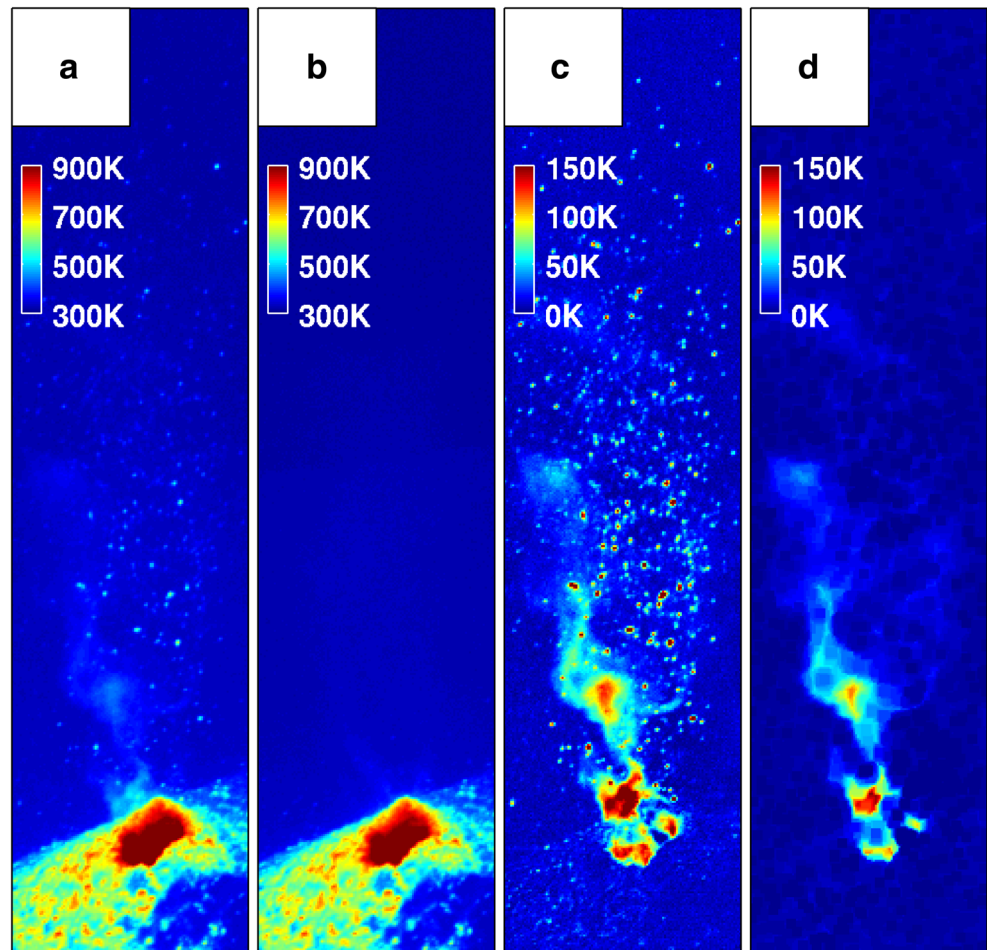
In the case of thin puffs, the absorbance is usually low (see "Use of thermal infrared imaging for puffing analysis"), and most of the electromagnetic signal recorded by the camera originates from the background. Thus, instead of  $L$ , we favor the use of the luminance anomaly  $\Delta L$ , which accounts for background effects:

$$\Delta L = L_{\text{cam}} - L_{\text{bg}} = (1 - \tau) (L_p - L_{\text{bg}}) \quad (4)$$

In practice, we assume that puffs are hot transients crossing a colder background (Fig. 2a) so that  $L_{\text{bg}}$  can be computed as the minimum value each pixel reaches over time, i.e., when it is not occupied by a puff. In order to minimize the effects of slow changes due to, e.g., clouds and rock falls,  $L_{\text{bg}}$  is computed as the minimum value of each pixel in a moving window of 2 s preceding each frame (Fig. 2b).  $L_{\text{bg}}$  is then removed from each frame to compute the luminance anomaly  $\Delta L$  associated with puffs (Fig. 2c). Similarly, hot bombs simultaneously ejected with the puffs can be removed from the frames by applying a low-pass spatial filter (Fig. 2d). This filter retains only the minimum luminance in square areas larger than the largest bomb, on the assumption that the high-luminance pixels in the square are occupied by hot bombs while lower ones represent colder puff. This last correction may crop the border of the puff and must be taken into account in size and volume estimations.

The preprocessed movies show  $\Delta L(x,y,t)$ , i.e., the time evolution of the luminance anomaly as a function of the horizontal and vertical coordinates of the image. For a more straightforward interpretation of the values, we use the brightness temperature instead of the luminance. Although there is a direct bijection between the two notations through Planck's law, calculations must be carried out on the luminance and then converted to  $T_b$  (Harris 2013). For instance, in order to compute the brightness temperature anomaly, we first convert the puff and background measured temperatures to luminance, compute the difference, and then convert back to brightness temperature anomaly. These intermediate steps are implicitly achieved for each of the calculations of this paper.

**Fig. 2** Preprocessing steps of the raw images for vent activity C14b (see details in the text). **a** Raw image of the brightness temperature ( $T_b$ ). **b** Image background ( $T_{b_{bg}}$ ), defined as the minimum value of the temperature recorded in the two previous seconds. **c** Brightness temperature anomaly ( $\Delta T_b = T_b - T_{b_{bg}}$ ). The signal is mostly acquired from the moving objects (gas and pyroclasts). **d** Brightness temperature anomaly after low-pass spatial filtering. The bombs have been removed



### Puff detection and characteristics

Puff ejection is marked by an increase of the brightness temperature above the vent. In previous thermal imaging studies, puffs were identified by detecting a single, averaged temperature anomaly above the vent (Harris and Ripepe 2007; Branam et al. 2008; Bani et al. 2013). In Fig. 3a, we present an original method to detect and measure the temperature anomaly generated by the puffs. The algorithm first detects the largest puff, corresponding to the highest peak on the whole dataset. Then, it finds the temporal/spatial extent or “region of influence” of this puff (in color in Fig. 3a), which, for each point of the curve, corresponds to the value of the local minimum (lowest valley) between this point and the highest peak. The region of influence of the largest puff is then subtracted from the curve, and the second-largest peak is detected in the residual. The process is iteratively repeated until the residual vanishes.

However, this method does not allow the detection of multiple puffs ejected at the same time or computing puff width or precise release point within the vent. We thus adapted this method by considering the time evolution of the brightness

temperature anomaly not on a point but on a horizontal detection line above the vent  $\Delta T_{b_y}(x,t)$ . In Fig. 3b, the horizontal and vertical axes represent respectively the time and the position on a horizontal line above the vent. As in 1-D, the highest peak is detected and the region of influence is computed and removed, and the process is iteratively repeated. The width and duration of the puffs can be directly estimated on the  $\Delta T_{b_y}(x,t)$  diagram (Fig. 3b). However, their precise measurement is not trivial because (1) puff boundaries get blurred by the interaction with the surrounding atmosphere and (2) neighboring puffs can merge. A first method to estimate objectively the width and duration of individual puffs using the  $\Delta T_{b_y}(x,t)$  diagram is to first integrate the thermal anomaly of the whole region of influence of a puff and then divide it by the maximum anomaly of the same puff (ratio method). However, this method is less effective when multiple puffs are merging. In such cases, a second, possibly more robust method is to define the width and duration of a puff as the area in Fig. 3 where  $\Delta T_{b_y}(x,t)$  couples have a luminance anomaly  $\geq 50\%$  the peak anomaly (threshold method). The center of this area defines the source time and location of the puff. Convergence of the two methods for a wide range of temperature distribution (6%

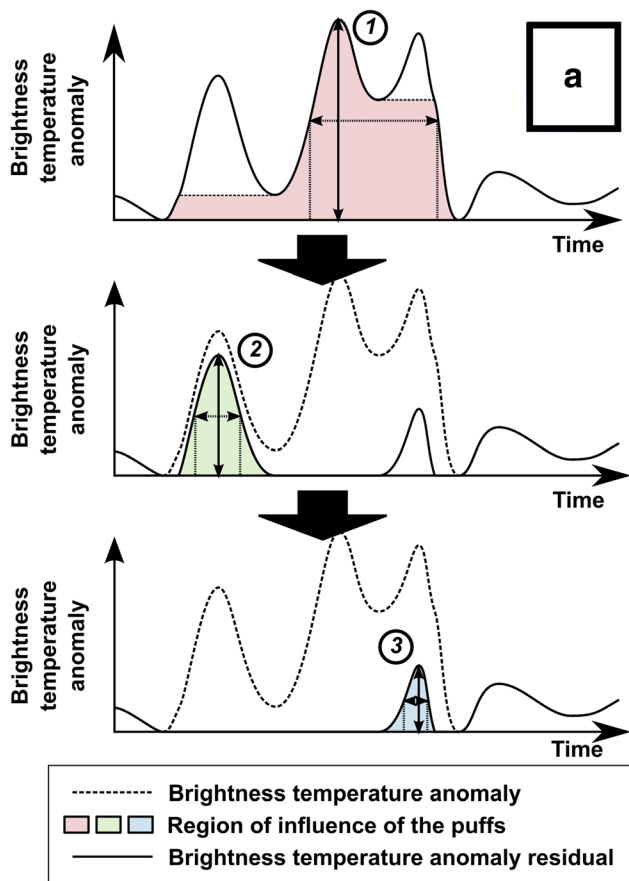
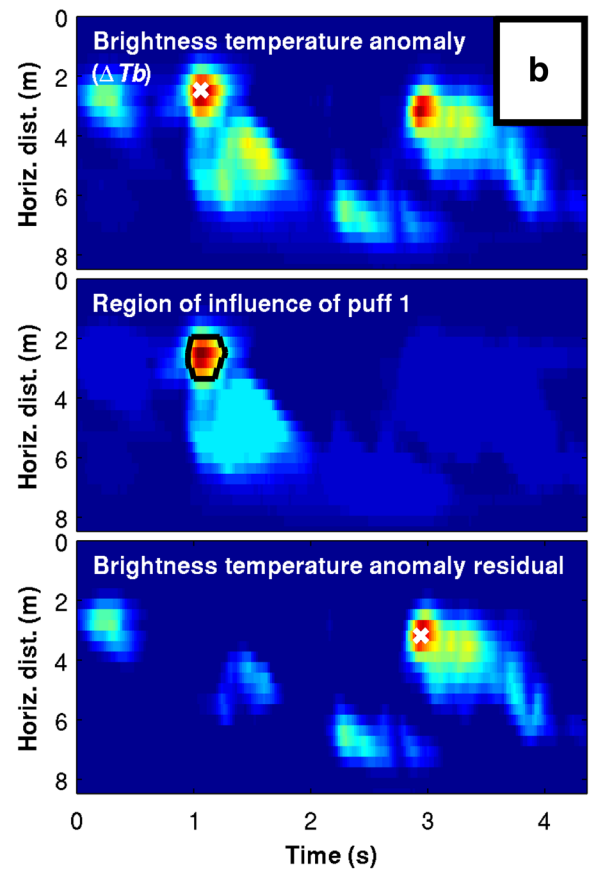


**Fig. 3** Puff detection algorithm. **a** Example of algorithm application for a single time series. From the brightness temperature anomaly, the highest peak is sought. The region of influence of each peak corresponds to the colored area, while the puff dimensions obtained using the threshold method correspond to the all the points having a brightness temperature anomaly  $\geq 50\%$  of the peak (*top panel*). The influence region is subtracted from the brightness temperature anomaly to compute the residual (*mid*

difference for normal distribution, 1% for a triangular, and 0% for a Heaviside distribution) give us confidence in our puff sizing capability.

False positive puff detections are removed by a final post-processing step. First, anomalies lower than a fixed threshold corresponding to the instrumental noise, smaller than two pixels, or lasting less than two frames are rejected. Then, we apply the detection algorithm on the pixel rows directly above and below the detection line, rejecting anomalies that are not detected on all the three successive rows. This last step also enables the estimation of the rise velocity of puffs through the delay in their arrival time at two successive rows, while uncertainties of the puff parameters estimations can be assessed by comparing the estimates on the three successive rows.

The final output of the algorithm is a database of the puffs with their time and position of emission, maximum brightness temperature anomaly, width  $w$ , duration  $d$ , and rise velocity  $v$  ([Supplementary material](#)). From the three latter parameters,



*panel*) until the smallest puffs are identified (*lower panel*). **b** Bi-dimensional application of the method on a  $\Delta T b_s(x,t)$  for vent activity C12c. On the *top panel*, the white cross represents the maximum temperature anomaly residual. On the *middle panel*, the region of influence spreads through the whole time window. In contrast, the threshold method enables a reliable estimate of the puff dimensions (*black line*)

the volume of each puff  $V$  can be estimated, assuming a spheroid shape where the depth equals the width:

$$V = \frac{\pi w^2 v}{6 d} \tag{5}$$

### Puff rise and dissipation

In order to study the rise and dissipation of the puffs, we consider the evolution of the brightness with time and height  $\Delta T b(y,t)$ . This analysis is done by retaining, for each frame, the maximum value for each row of the image and can be used to visualize the evolution of the brightness temperature anomaly over time and elevation above the vent.

In addition, we monitored the evolution of a few selected well-defined puffs by measuring on the successive frames their maximum temperature and their dimensions (height and width), based on the ratio method. The rise velocity is

estimated by measuring the displacement of the puff center in successive frames.

## Results

### Overview of puffing activity

Figure 4 shows 7 min of the activity of vent activity NE14c in a time/vertical position (or rise history) diagram  $\Delta Tb(y,t)$ , without low-pass spatial filtering, showing the pulsating ejection and rise of puffs. The blurred limits of the traces indicate their gaseous nature, while their curved slopes reflect a slightly decreasing rise velocity. Puffing activity at one vent, defined by the frequency and the brightness temperature anomaly of puffs, changes on a timescale of minutes. For instance, strong activity is observed between 14:20:25 GMT and 14:21:00 GMT while activity is minimal between 14:24:40 and 14:25:20 GMT.

For this reason, we illustrated the variety of puffing activity by “snapshots,” i.e., representative, 1-min-long rise history diagrams of eight different vents activities (Fig. 5 and Table 1). Out of the three (2012), four (2013), and seven

(2014) vents hosting puffing activity in 2012, 2013, and 2014, respectively, two, one, and five were suitable for video analysis. Puffing activity varies largely in (1) the intensity of the brightness temperature anomaly, (2) puff dimensions, (3) altitude at which puffs dissipate, and (4) temporal distribution of the puff emissions. In three cases (SW14e, SW14d, C14b), parabolas on the diagram highlight the ejection of bombs at velocities up to  $30 \text{ m s}^{-1}$  simultaneously with the puffing. Due to the large number of bombs erupted, C14b can be classified as “rapid Strombolian explosions” according to Houghton et al. (2016) definition. However, the same detection and processing algorithms can be applied, and vent C14b is treated as an extreme case of puffing hereafter. The time/horizontal position (or vent history) diagram  $\Delta Tb_x(x,t)$  of the same representative intervals highlights the large discrepancies in terms of puff width (Fig. 6). In particular, the smallest puffs are smaller than the vent diameter. Interestingly, several puffs appear to be released simultaneously from slightly different points within the same vent, in particular at the most active vents. The effect of wind is also clearly visible (e.g., C13b), quickly dispersing the puffs laterally.

### Individual puff characteristics

The detection algorithm provided the parameters for 607 individual puffs from the eight snapshots of vent activities (between 20 and 136 puffs per case, see Table 1). The efficiency of the algorithm can be visually assessed by plotting the automatically detected puff time and location in Fig. 6. The error associated with each measurement (Supplementary material) demonstrates the excellent reliability of the algorithm to estimate the temperature anomaly, duration, and width of each puff. Only the rise velocity is subject to high uncertainties due to the computation technique, and some of the estimates appear unrealistic. Thus, to compute volumes, we use the same rise velocity estimate for all the puffs of a given vent, corresponding to the median value of the rise velocities.

From these databases, we can parameterize and explore the variability of puffing parameters at Stromboli. Despite the large variety of puffing activity, the brightness temperature anomaly generated by a puff relates to its dimensions by a power law:

$$\Delta Tb = \varepsilon X^\eta \tag{6}$$

$X$  representing either the width or the volume of the puff (Fig. 7). The constant  $\varepsilon$  characterizes well each snapshot, while the exponent  $\eta$  is independent of the case, close to 1 for the radius and 1/3 for the volume. No clear relationship links exit velocity and volume or brightness temperature of puffs.

The time interval between two successive puffs for each minute-snapshot (inter-puff time) is represented in Fig. 8. On the three most active cases (C14b, SW14d, and C13b), the

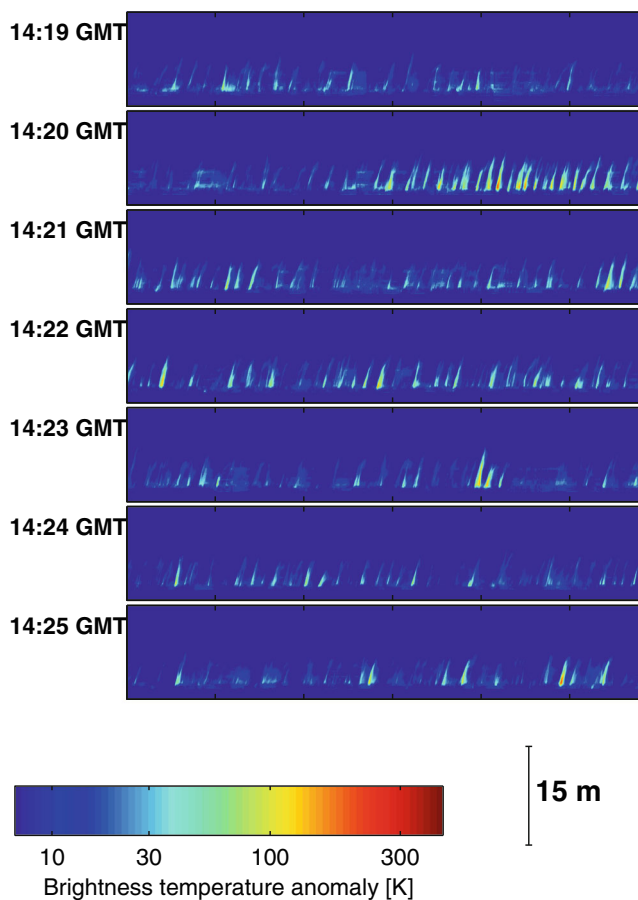


**Fig. 4** Time evolution of the brightness temperature anomaly  $\Delta Tb(y,t)$  above the vent NE14c during a 7-min record, showing seconds-scale variations in puffing activity

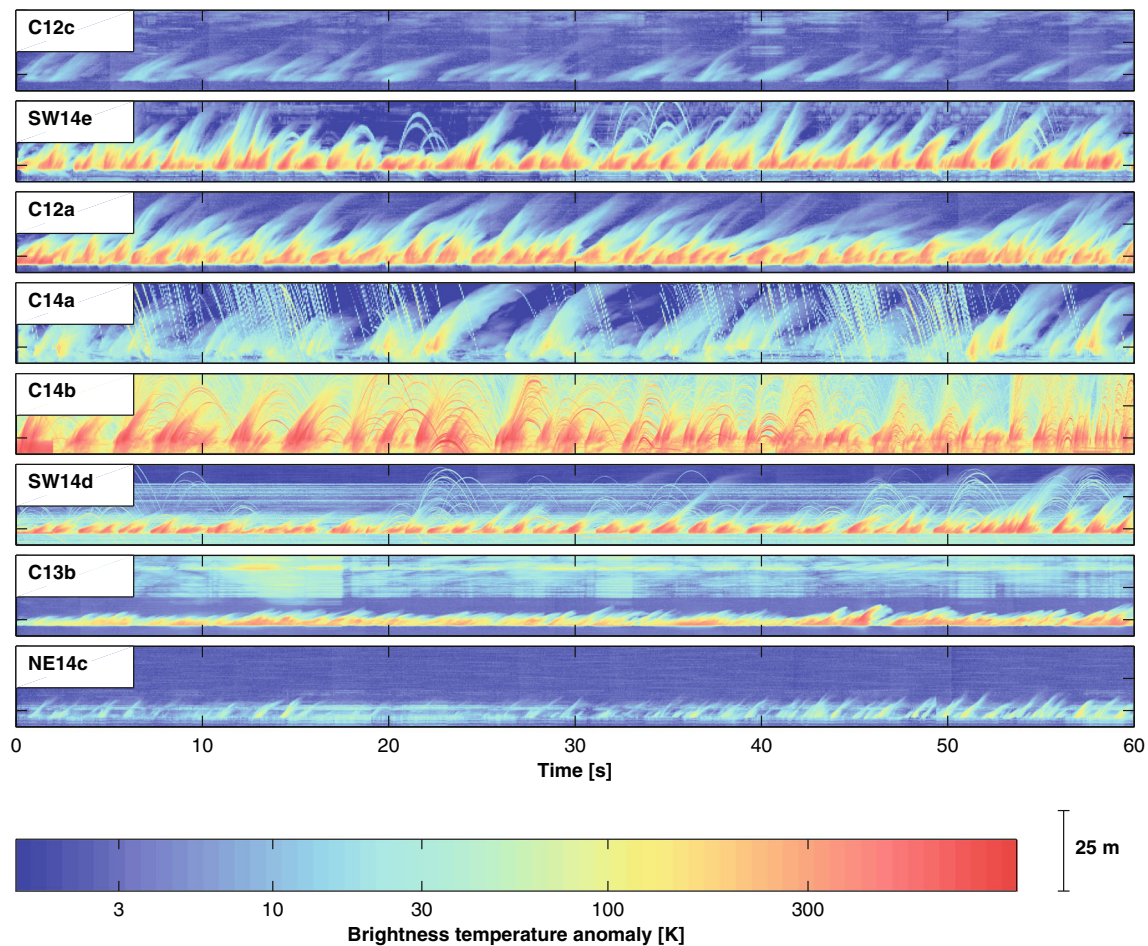


**Fig. 5** Rise history diagram  $\Delta T_b(y,t)$  representative of 1 min of vent activities. The *parabolas* correspond to the ballistic trajectories of the bombs while the *blurred traces* are representative of the buoyant

material erupted (gas and potentially ash). (Note that, on vent activity C14a, the *downward tracks* correspond to bombs that were ejected from the neighbor vent C14b)

survival function of the inter-puff time follows a power distribution (Fig. 8a), suggesting that gas releases are randomly distributed. Conversely, for the other five snapshots of the vent activity, the trend is non-linear. The linear part points toward a minimum delay between two successive puffs, ranging between 0 and 0.5 s and characterizing each case. These latter, less active vent activities also display a correlation between the inter-puff time and the brightness temperature anomaly of the following puffs (Fig. 8b), which is not present for the former three vent activities.

This contrast between high activity and low activity vents is also visible in the puffing frequency and puffs size (Fig. 9). Vent activities with a higher repetition rate of puffs also display stronger brightness temperature anomalies.

### Puff rise and dissipation

Once released, the thermal signature of the puffs dissipates while the puffs rise and mix with the surrounding atmosphere.

Qualitatively, cooling is relatively fast, with most puffs being no longer thermally detectable 20 m above the vent (Fig. 6). This cooling is generally associated with a decrease of their rise velocity over time.

In order to quantify these observations, we selected and tracked over time the rise velocity, maximum brightness temperature anomaly, and radius of 6 well-defined, isolated puffs from vent activity SW13d (Fig. 10). In all six cases, the radius is stable or even slightly decreasing in the first 4 m above the vent and then increases with the height at a ratio, corresponding to an air entrainment coefficient (Morton et al. 1956) ranging between 0.045 and 0.14. The maximum brightness temperature anomaly decreases as a power function of the height, getting divided by 2 each 1.0 to 2.2 m. Finally, the rise velocity is either stable or decreasing over height. While the initial rise velocity is not linked to the brightness temperature anomaly, there is a clear positive correlation between volume, temperature, and terminal rise velocity.

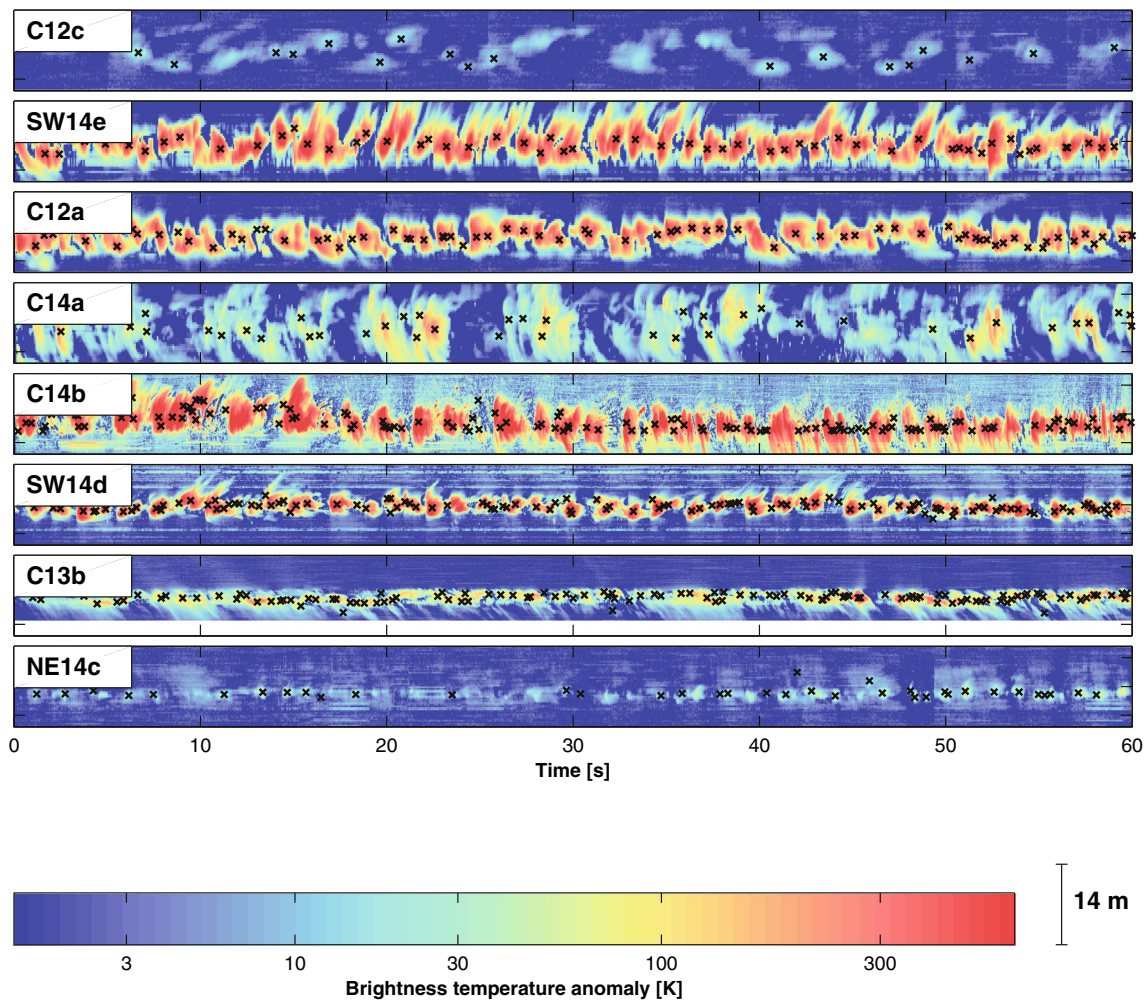


**Fig. 6** Vent history diagram  $\Delta T_{b,y}(x,t)$  of the same vent activities as Fig. 4. The crosses correspond to the detected puffs, after post-processing

**Discussion**

Puffing has been observed in many open-vent basaltic volcanoes, such as Yasur (Bani et al. 2013; Spina et al. 2015),

Masaya (Branan et al. 2008), Villarica (Gurioli et al. 2008), and Stromboli (e.g., Ripepe and Gordeev 1999; Ripepe et al. 2002; Harris and Ripepe 2007; this study). It has been widely suggested that it is diagnostic of the conduit condition both at

**Fig. 7** Relationship between the brightness temperature anomaly and the size (a) and volume (b) of individual puffs for the different vent activities. In (b), note how temperature increases with increasing volume within one vent while it decreases with increasing volume when considering the different vents

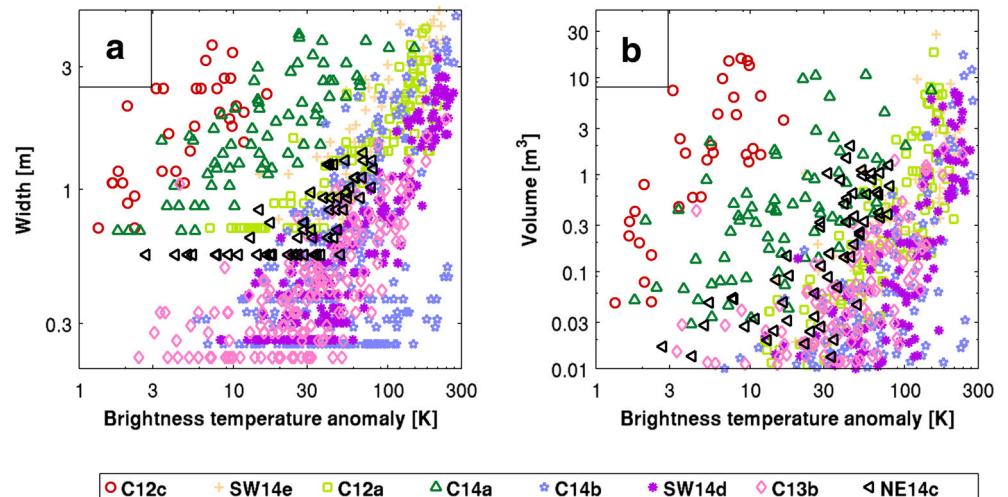
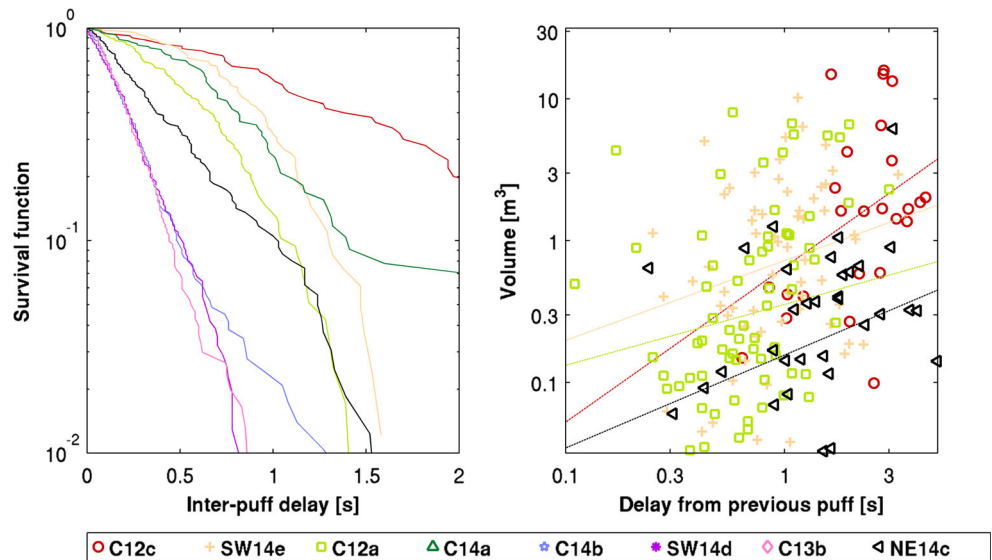


**Fig. 8** Inter-puff delay on the eight studied vent activities. *Left:* survival functions, representing for each vent the proportion of inter-puff times exceeding a given duration. Straight lines represent power law distribution. *Right:* relationship between the volume and the delay from the previous puff for the vent activities SW14e, C12a, NE14c, and C12c (there is no significant correlation for the four others)



depth (gas supply) and in the shallowest part of the plumbing system (e.g., Landi et al. 2011). Thus, a reliable parameterization of puffing activity is a crucial requirement to enable monitoring and comparison between volcanoes.

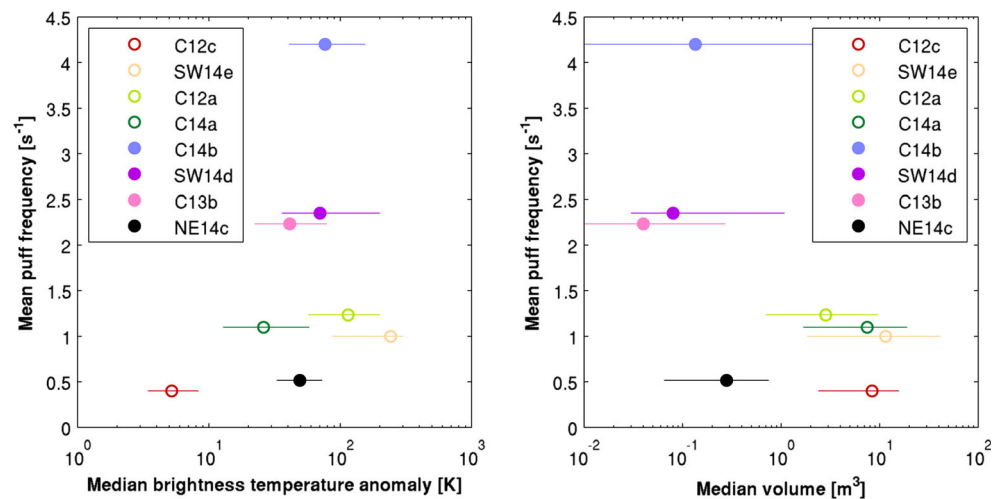
**Use of thermal infrared imaging for puffing analysis**

The methodology proposed here presents multiples advantages compared to the previous studies where a unique temperature was integrated over large field of view (Johnson et al. 2004; Harris and Ripepe 2007; Sahetapy-Engel et al. 2008; Bani et al. 2013). First, it facilitates the estimation of the gas velocity at the exit of the vent. The comparison of this velocity to the Stokes velocity could enable the identification of the occurrence of gas thrust generated by the overpressure of the gas pocket (Harris and Ripepe 2007). Second, measuring the temperature evolution just above the vent (Fig. 6) allows

capturing fine details before the merging of the puffs while the “integrated temperature” smooths the thermal signal, thus not allowing distinguishing puffs spaced by less than 0.5–1 s. Third, it allows a direct measurement of the puff width and volume without being influenced by the volume changes due to dilution in the atmosphere. In particular, it allows measuring the widths of the puffs, which do not necessarily correspond to the vent diameter, thus providing more reliable estimations of the individual puff volumes. Measuring puff characteristics on successive pixel rows within the image allow to estimate the uncertainties of our method, which is in most cases was smaller than 30%.

However, Fig. 5 clearly demonstrates that puffs parameters, and in particular the brightness temperature anomaly, rapidly change while the puff is rising. For case SW14d, it is divided by a factor of 2 each 1.0 to 2.2 m of ascent (Fig. 10a), so that the thermal signature usually vanishes after 20 m. Thus, it is

**Fig. 9** Average characteristics of puffing for the eight vent activities of this study. Error bars represent the first and the third quartile of the volume distribution



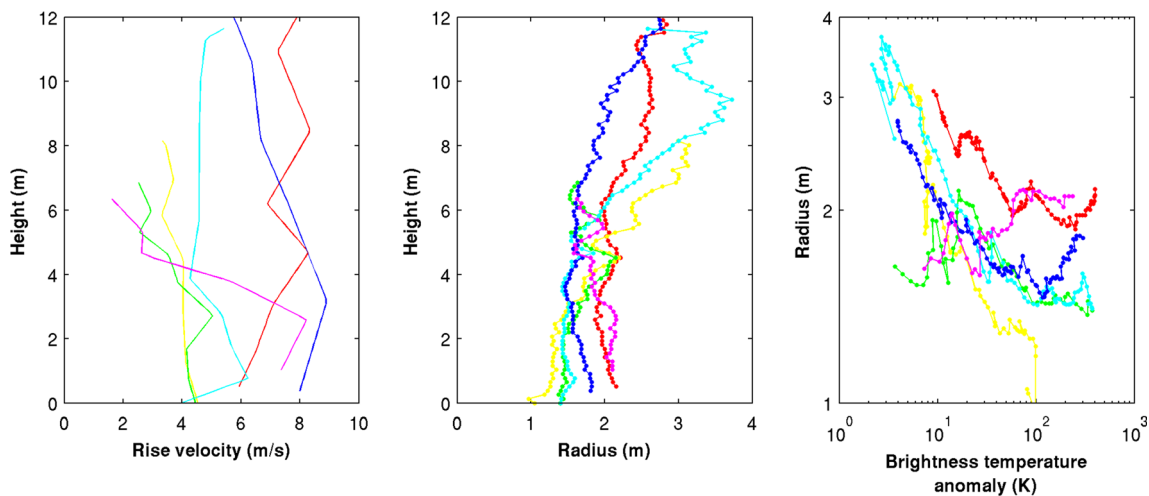


**Fig. 10** Evolution of the rise velocity, radius, and brightness temperature anomaly of six individual puffs during their rise from vent SW14d

crucial to estimate the variations of the puff parameters while it rises in order to assess the reliability of the measurements.

In order to interpret the cooling mechanism, we can first estimate the effect of the radiative transfer from a puff. For simplification, we consider a spherical isothermal blackbody with a radius  $r$  made of approx. 80% H<sub>2</sub>O and 20% CO<sub>2</sub> (Burton et al. 2007). The radiative flux can be computed through the Stefan-Boltzmann law and divided by the heat capacity of the puff:

$$\frac{dT}{dt} = - \frac{4\pi r^2 \sigma (T^4 - T_{atm}^4)(1 - \tau)}{\frac{4}{3}\pi r^3 \rho c} \quad (7)$$

where  $\sigma$  is the Stefan-Boltzmann constant ( $\sigma = 5.67 \times 10^5 \text{ W m}^{-2} \text{ K}^{-4}$ ),  $\rho$  the density of the puff ( $280 / T$ , in grams per cubic meter), and  $c$  its heat mass capacity ( $1.74 \text{ J K}^{-1} \text{ g}^{-1}$ ). For a 1-m-radius puff at 1000 K, the cooling rate is  $346 \text{ K s}^{-1}$ , which is slightly smaller than observed. Conversely, for cooler plumes, the rate is much lower ( $2.4 \text{ K s}^{-1}$  for a 1-m puff at 400 K) and is not compatible with the observations.

Another hypothesis for the cooling of the plumes is their dilution in the atmosphere. Figure 10b shows that puff radius does not vary significantly for the first 4 ca. meters of its ascent above the vent but later increases steadily with height according to Morton’s law (Morton et al. 1956). The measured air entrainment coefficients (0.045–0.14) correspond to the lower bound of previous studies of non-volcanic puffs (Scorer 1957; Turner 1979). Considering the late stage of puff rise and dispersion in Fig. 10c, we see a clear correlation between the decrease of brightness temperature anomaly and the radius increase in the form of:

$$\Delta T b = \varepsilon r^\eta \quad (8)$$

where  $r$  is the radius of the puff and  $\varepsilon$  and  $\eta$  are two constants. While  $\varepsilon$  depends on the puff,  $\eta$  is relatively stable and ranges

between  $-4.04$  and  $-5.37$ . The loss of temperature when the plume dilutes in the atmosphere can be estimated by considering a constant total heat of the plume distributed on a variable volume. Thus, we expect the temperature to vary as the inverse of the volume, that is to say the inverse cube of the radius ( $\eta = -3$ ). Taking into account the density variations and the changes of composition of the plume while it dilutes and cools down does not change significantly this estimation ( $\eta = -2.6$  to  $-3.1$ ).

As a consequence, in order to explain the high values of  $\eta$  observed, we have to consider the decrease of transmittance (Eq. (3)). Indeed, the gas concentration varies with the inverse cube of the radius. Consequently, for thin plumes, the transmittance can decrease with the inverse square of the radius. Thus, the exponent of Eq. (7) is expected to range between  $-3$  (for opaque plumes) and  $-5$  (for thin plumes), which corresponds to the observed range.

We conclude that the cooling of gas puffs is likely dominated by radiation on exiting the vent, while air entrainment and dilution dominate in a second step. However, the initial brightness temperature might be significantly increased by the presence of small pyroclasts, which cools slower than the puff while increasing its absorbance. The decoupling of these small pyroclasts from the puffs may enhance the temperature drop.

The linear relationship between puff radius and brightness temperature above the vent (Fig. 7b) suggests that the real gas temperature at the exit of the vent is independent of puff size and the brightness temperature depends only on the transmittance of the puff. A corollary of this observation is that puffs may not cool down significantly during their rise in the conduit, i.e., their temperature at the vent may be a good proxy for the temperature of gas in the magma. However, the scaling factor  $\varepsilon$  is strongly depending on the puff (Figs. 7 and 10), preventing the extraction of quantitative data. Potentially, multispectral thermal infrared observations could allow the retrieval of the transmittance of a puff and the derivation of

its absolute temperature. Such techniques are routinely used for retrieving the emissivity of the surfaces (Gillespie et al. 1998; Rose et al. 2014) or the CO<sub>2</sub> and ash contents of volcanic plumes (Corradini et al. 2009).

Here, we could provide rise-dependent parameters only for a limited case when puffing rates are low. In the case of frequent puffing, closely spaced puffs are too complicated to be effectively followed, since they interact with one another in complex ways. Indeed, the bottom boundary of the puffs is usually more blurred than the upper one (Fig. 5), highlighting the presence of turbulence at the base of the puffs. This turbulence may reduce the drag for the following puff, thus enhancing the merging of multiple puffs. These effects characterize the puffing dynamics in the majority of the cases we observed.

### Variability of puffing and vent conditions

A large variety of puffing activity can be observed while comparing Stromboli to other volcanoes. First, the puff rate, ranging from 20 to 136 burst/min, remains high compared to the estimations at other volcanoes: 6–8 burst/min at Masaya (Branan et al. 2008), 9 burst/min at Villarica (Gurioli et al. 2008), or between 1 and 2 bursts/min (Bani et al. 2013) and 40 burst/min (Spina et al. 2015) at Yasur. Conversely, the size of puffs (typically 0.1 to 10 m<sup>3</sup>) is smaller than what is observed at Masaya (typically 1000–10,000 m<sup>3</sup>). This anti-correlation between the puffing rate and the average volumes could be a consequence of the conduit diameter, larger conduits enabling larger gas pockets to rise.

Even at the scale of the volcano, a large variety can be observed, that might reflect changes in the shallow conduit system. At Stromboli, puffing ranges from low temperature–low rate end-members (e.g., C12c, 20 puffs per minute, average temperature anomaly 3 K) to high temperature–high rate ones (e.g., C14b, 136 puffs per minute and up to 600 K, Fig. 9), from puffing with or without the simultaneous ejection of pyroclasts (with ejection in three cases out of eight, Fig. 6), and with intra-vent puffing variability at the timescales of tens of seconds to minutes (Fig. 5). This large variability of puffing activity, possibly emerging today thanks to a combination of new data collection/analysis techniques and fortuitous volcanic activity, has implications for both future remote sensing of volcanic activity at Stromboli and for shallow conduit dynamics at basaltic volcanoes. If puffing is related to the burst of small, pressurized gas bubbles close to the surface (Ripepe et al. 1996), such bubbles appear to occur in a range of sizes and the released gas to reach the surface in a variety of temperature/pressure/dilution conditions.

Puffs allow us to infer the vent section, which may be defined as the narrow band of a few meters from which puffs are emitted for each vent (Fig. 6). While the largest puffs completely fill this section (and hence the whole shallow

conduit), smaller puffs appears to be smaller than the section, allowing in rare cases the simultaneous emission of two puffs from the same vent. This implies that (i) bursting bubbles may be significantly narrower than the slugs that usually fill most of the conduit diameter and (ii) the gas released by each burst does not expand to fill the whole conduit. In agreement, the height to width ratio of puffs suggests that they do not significantly elongate in the conduit like the slugs as the origin of normal Strombolian activity. Finally, on vent activities ejecting pyroclasts together with puffs (SW14d, SW14e, C14b), backtracking pyroclasts trajectories indicates a source located between 2 and 10 m below the surface, coincident with the depth computed for Strombolian explosions (Gaudin et al. 2014).

Although our puff volume estimates being in excellent agreement with those from peak infrasonic pressure (Ripepe and Gordeev 1999), the observed inter-puff delay time are, in our case, not constant but rather a random process mostly characterized by an exponential trend on a survival function diagram (Fig. 7). Only in the less active cases are such functions kinked, the linear part pointing to a minimum delay between successive puffs of up to 0.5 s. Such offset random distribution has been observed in numerous repetitive explosive processes and has been interpreted experimentally as a consequence for bubble coalescence in the conduit (Toramaru 1989; Ripepe et al. 2002; Pering et al. 2015). In addition, less frequent vent activities show a direct relationship between inter-puff time interval and puff volume and apparent temperature, while this relationship tends to be lost by more active vents (possibly because high puffing rates increasingly hinder distinguishing individual puffs). The inter-puff delay and the size distribution of the puffs are related to bubble expansion and coalescence within the magma column (Ripepe and Gordeev 1999). Since highest frequencies are linked to higher apparent temperature and smaller puff volumes, we hypothesize that they are linked to higher number of smaller bubbles and overall magma rise velocities, limiting the effect of free coalescence. Conversely, for less active vents, lower bubble numbers and magma ascent velocity allows coalescence by differential rise to play a stronger role. It is also possible that, depending on shallow magma conditions at a vent, a lower threshold of gas volume, i.e., a minimum amount of coalescence, controls the eruption of puffs. This lower threshold could be linked, for instance, to the buoyancy required to penetrate the shallow, more viscous layers of the magma column (Gurioli et al. 2014; Del Bello et al. 2015; Capponi et al. 2016) or debris cover on top of the vent (Leduc et al. 2015). Additional investigation on other volcanoes will be required to validate or refute this hypothesis. A further interpretation of this minimum inter-puff delay is also made difficult by the lack of experimental and/or numerical studies on the rise of gas pockets in a conduit with the same size.

## Puffing location and volcano activity

Puffing location within the crater terrace has been considered to be diagnostic of magma circulation in the shallow plumbing system (Ripepe et al. 2009; Landi et al. 2011). Vents featuring puffing activity host hotter magma than other vents (Landi et al. 2011) because bubbles rise more easily in the less viscous magma or/and because magma circulation and heat advection is promoted by bubbles. At Stromboli, they are located mostly—but not only—in the central vent area (Harris and Ripepe 2007; Ripepe et al. 2007, 2009; Spampinato et al. 2012). Changes in the convection pattern within a NE-SW elongated system would shift the magma–gas streamlines and cause changes in the location of puffing from one to another vent area (Ripepe et al. 2009). Although our coverage supports the dominance of the central vent area as the main source of puffing (Table 1), we also found simultaneous puffing at multiple vents in all years and from all vent areas, in contrast with previous studies (Harris and Ripepe 2007; Ripepe et al. 2007, 2009; Spampinato et al. 2012). For instance, summarizing nine field campaigns between 1994 and 2004, Harris and Ripepe (2007) never describe simultaneous puffing at multiple vents, not even when puffing activity shifted from one to another vent. Our observations suggest complex magma and gas circulation below the vents.

We also note that increasing puffing activity observed during the field missions, from three to four puffing vents in 2012–2013 to seven puffing vents in 2014, corresponds to an increase in the hourly rate of Strombolian explosions from 9 to 13 to 17. Also, gas fluxes observed at vents, estimating by summing the contribution of each individual puffs were high ( $>50 \text{ m}^3 \text{ s}^{-1}$ ), corresponding to the higher estimates of Tamburello et al. (2012) ( $0.27 \text{ kg SO}_2/\text{s}$ ), while in 2012, the gas flux from puffing was only  $10 \text{ m}^3 \text{ s}^{-1}$ . Notably, in 2014, magma level was so high that effusive activity occurred within the crater terrace only a few weeks after our field campaign. These broad relationships reveal how increasing gas fluxes and decreasing magma viscosity in the shallow plumbing system do not limit their effects to shifting puffing from one vent area to another but also activate puffing conditions at a larger number of vents.

## Conclusion

Thanks to its persistent and common occurrence, puffing potentially offers an ideal tool to monitor the thermal and degassing state of magma at open-vent volcanoes, with implications for both hazard mitigation and environmental assessment. However, exploitation of the full monitoring potential of puffing has two key requisites. First, we need a tool to detect and measure puffing efficiently. Second, we need an

interpretative framework linking puffing and magma degassing/explosive activity.

The use of infrasound allows monitoring regardless of the meteorological conditions, but may be limited in case of multiple vents being active at the same time. In this scope, the development of new, high-speed high-resolution thermal cameras allowing to observe and describe individual puffs is a complementary technique not only allowing to discriminate precisely which vent is hosting puffing but also characterizing the puffing activity itself. In this scope, the development of an objective method to individuate and measure individual puffs from thermal high-speed videos regardless of vent characteristics and conditions is an indispensable prerequisite to characterize and compare puffing characteristics at different times and vents.

The application of our original algorithm at Stromboli allowed us to observe brightness temperature anomalies spread over more than two orders of magnitude, from the detection limit of the system (3 K) to temperatures (600 K) approaching magmatic ones. Observed puffing frequencies (from 20 to 136 puffs per minute) spread the range observed in other volcanoes: 6–8 burst/min at Masaya (Branan et al. 2008), 9 burst/min at Villarica (Gurioli et al. 2008), or 40 burst/min (Spina et al. 2015) at Yasur. Similarly, volume estimates of individual puffs, usually in the range  $0.1\text{--}10 \text{ m}^3$  at Stromboli, allow an independent estimate of the volumetric flux of gas, in excellent agreement with previous studies that use different observation techniques (e.g., Tamburello et al. 2012). Indeed, the next step will be coupling our thermal infrared perspective with other monitoring systems, first of all UV imaging and infrasonic recording.

We suggest that the number of vents that simultaneously host puffing reflects the general intensity of volcanic activity as expressed by, e.g., the frequency of Strombolian explosions. At a deep level, the amount of puffing reflects the overall gas flux of a volcano. At a shallower level, the smaller and more frequent puffing at “hotter” vents is in agreement with rapid rise of small bubbles with only limited coalescence, while slower rise, allowing more time for coalescence, leads to larger but less frequent puffing at “colder” vents. This link between puffing style and vent thermal state points to a feedback between gas flux and magma temperature (and viscosity), where higher gas flux stirs and heats the magma, which, by getting less viscous, becomes a preferential way for bubble rise. In this scope, the monitoring of puffing appears to be a simple and highly relevant method for determining the state of activity of a volcano.

**Acknowledgments** The research leading to these results has received funding from the People Programme (Marie Curie Actions) of the European Union’s Seventh Framework Programme (FP7/2007–2013) under the project NEMOH, REA grant agreement no. 289976, the INGV-DPC “V2,” “Paroxysm,” and “MIUR-PREMIALE 2012 NORTH Nuovi orizzonti tecnologici per la ricerca sperimentale e il monitoraggio

geofisico e vulcanologico” projects. We acknowledge Andrew McGonigle, Steve Lane, and an anonymous reviewer, as well as Josef Dufek and James White for their excellent comments that helped improving the quality of this paper! Grazie mille !

## References

- Allard P, Carbonnelle J, Métrich N, Loyer H, Zettwoog P (1994) Sulphur output and magma degassing budget of Stromboli Volcano. *Nature* 368:326–330. doi:10.1038/368326a0
- Bani P, Harris AJL, Shinohara H, Donnadieu F (2013) Magma dynamics feeding Yasur’s explosive activity observed using thermal infrared remote sensing. *Geophys Res Lett* 40:3830–3835. doi:10.1002/grl.50722
- Barberi F, Rosi M, Sodi A (1993) Volcanic hazard assessment at Stromboli based on review of historical data. *Acta Vulcanol* 3: 173–187
- Berk, A., Bernstein, L.S., Robertson, D.C., 1987. MODTRAN: a moderate resolution model for LOWTRAN. DTIC Document
- Branan YK, Harris A, Watson IM, Phillips JC, Horton K, Williams-Jones G, Garbeil H (2008) Investigation of at-vent dynamics and dilution using thermal infrared radiometers at Masaya Volcano. *Nicaragua J Volcanol Geotherm Res* 169:34–47. doi:10.1016/j.jvolgeores.2007.07.021
- Burton M, Allard P, Muré F, La Spina A (2007) Magmatic gas composition reveals the source depth of slug-driven strombolian explosive activity. *Science* 317:227–230. doi:10.1126/science.1141900
- Capponi A, James MR, Lane SJ (2016) Gas slug ascent in a stratified magma: implications of flow organisation and instability for strombolian eruption dynamics. *Earth Planet Sci Lett* 435:159–170. doi:10.1016/j.epsl.2015.12.028
- Cerminara M, Esposti Ongaro T, Valade S, Harris AJL (2015) Volcanic plume vent conditions retrieved from infrared images: a forward and inverse modeling approach. *J Volcanol Geotherm Res* 300:129–147. doi:10.1016/j.jvolgeores.2014.12.015
- Chandrasekhar, S., 1960. Radiative transfer. Courier Dover Publications
- Corradini S, Merucci L, Prata AJ (2009) Retrieval of SO<sub>2</sub> from thermal infrared satellite measurements: correction procedures for the effects of volcanic ash. *Atmos Meas Tech* 2:177–191. doi:10.5194/amt-2-177-2009
- Del Bello E, Lane SJ, James MR, Llewellyn EW, Taddeucci J, Scarlato P, Capponi A (2015) Viscous plugging can enhance and modulate explosivity of strombolian eruptions. *Earth Planet Sci Lett* 423: 210–218. doi:10.1016/j.epsl.2015.04.034
- Del Bello E, Llewellyn EW, Taddeucci J, Scarlato P, Lane SJ (2012) An analytical model for gas overpressure in slug-driven explosions: insights into strombolian volcanic eruptions. *J Geophys Res Solid Earth* 117(B02206). doi:10.1029/2011JB008747
- Gaudin D, Taddeucci J, Scarlato P, Moroni M, Freda C, Gaeta M, Palladino DM (2014) Pyroclast tracking velocimetry illuminates bomb ejection and explosion dynamics at Stromboli (Italy) and Yasur (Vanuatu) volcanoes. *J Geophys Res Solid Earth* 119: JB011096. doi:10.1002/2014JB011096
- Gillespie A, Rokugawa S, Matsunaga T, Cothorn JS, Hook S, Kahle AB (1998) A temperature and emissivity separation algorithm for Advanced Spaceborne Thermal Emission and Reflection Radiometer (ASTER) images. *IEEE Trans On Geosci Remote Sens* 36(4):1113–1126. doi:10.1109/36.700995
- Gurioli L, Colo L, Bollasina AJ, Harris AJL, Whittington A, Ripepe M (2014) Dynamics of strombolian explosions: inferences from field and laboratory studies of erupted bombs from Stromboli Volcano. *J Geophys Res Solid Earth* 119(2013):JB010355. doi:10.1002/2013JB010355
- Gurioli L, Harris A, Houghton BF, Polacci M, Ripepe M (2008) Textural and geophysical characterization of explosive basaltic activity at Villarrica Volcano. *J Geophys Res* 113:B08206. doi:10.1029/2007JB005328
- Harris, A., 2013. Thermal remote sensing of active volcanoes: a user’s manual. Cambridge University Press. doi: 10.1017/CBO9781139029346
- Harris A, Ripepe M (2007) Temperature and dynamics of degassing at Stromboli. *J Geophys Res Solid Earth* 112:B03205. doi:10.1029/2006JB004393
- Houghton BF, Taddeucci J, Andronico D, Gonnermann HM, Pistolesi M, Patrick MR, Orr TR, Swanson DA, Edmonds M, Gaudin D, Carey RJ, Scarlato P (2016) Stronger or longer: discriminating between Hawaiian and strombolian eruption styles. *Geology* G37423:1. doi:10.1130/G37423.1
- James MR, Lane SJ, Corder SB (2008) Modelling the rapid near-surface expansion of gas slugs in low-viscosity magmas. *Geol Soc Lond Spec Publ* 307:147–167. doi:10.1144/SP307.9
- Johnson JB, Harris AJL, Sahetapy-Engel STM, Wolf R, Rose WI (2004) Explosion dynamics of pyroclastic eruptions at Santiaguito Volcano. *Geophys Res Lett* 31:L06610. doi:10.1029/2003GL019079
- Landi P, Marchetti E, La Felice S, Ripepe M, Rosi M (2011) Integrated petrochemical and geophysical data reveals thermal distribution of the feeding conduits at Stromboli Volcano. *Italy Geophys Res Lett* 38:L08305. doi:10.1029/2010GL046296
- Leduc L, Gurioli L, Harris A, Colò L, Rose-Koga EF (2015) Types and mechanisms of strombolian explosions: characterization of a gas-dominated explosion at Stromboli. *Bull Volc* 77(1):1–15. doi:10.1007/s00445-014-0888-5
- Morton BR, Taylor G, Turner JS (1956) Turbulent gravitational convection from maintained and instantaneous sources. *Proc R Soc Lond Math Phys Eng Sci* 234:1–23. doi:10.1098/rspa.1956.0011
- Oppenheimer C, Bani P, Calkins JA, Burton MR, Sawyer GM (2006) Rapid FTIR sensing of volcanic gases released by strombolian explosions at Yasur Volcano. *Vanuatu Appl Phys B* 85:453–460. doi: 10.1007/s00340-006-2353-4
- Pering TD, Tamburello G, McGonigle AJS, Aiuppa A, James MR, Lane SJ, Sciotto M, Cannata A, Patanè D (2015) Dynamics of mild strombolian activity on Mt. Etna. *J Volcanol Geotherm Res* 300: 103–111. doi:10.1016/j.jvolgeores.2014.12.013
- Planck M (1901) On the law of distribution of energy in the normal spectrum. *Ann Phys* 4:1
- Ripepe M, Delle Donne D, Lacanna G, Marchetti E, Olivieri G (2009) The onset of the 2007 Stromboli effusive eruption recorded by an integrated geophysical network. *J Volcanol Geotherm Res, The 2007 Eruption of Stromboli* 182:131–136. doi:10.1016/j.jvolgeores.2009.02.011
- Ripepe M, Gordeev E (1999) Gas bubble dynamics model for shallow volcanic tremor at Stromboli. *J Geophys Res Solid Earth* 104: 10639–10654. doi:10.1029/98JB02734
- Ripepe M, Harris AJL, Carniel R (2002) Thermal, seismic and infrasonic evidences of variable degassing rates at Stromboli Volcano. *J Volcanol Geotherm Res* 118:285–297. doi:10.1016/S0377-0273(02)00298-6
- Ripepe M, Marchetti E, Olivieri G (2007) Infrasonic monitoring at Stromboli Volcano during the 2003 effusive eruption: insights on the explosive and degassing process of an open conduit system. *J Geophys Res Solid Earth* 112:B09207. doi:10.1029/2006JB004613
- Ripepe M, Poggi P, Braun T, Gordeev E (1996) Infrasonic waves and volcanic tremor at Stromboli. *Geophys Res Lett* 23:181–184. doi: 10.1029/95GL03662
- Rose SR, Watson IM, Ramsey MS, Hughes CG (2014) Thermal deconvolution: accurate retrieval of multispectral infrared emissivity from thermally-mixed volcanic surfaces. *Remote Sens Environ* 140: 690–703. doi:10.1016/j.rse.2013.10.009

- Rosi M, Bertagnini A, Landi P (2000) Onset of the persistent activity at Stromboli Volcano (Italy). *Bull Volcanol* 62:294–300. doi:10.1007/s004450000098
- Sahetapy-Engel ST, Harris AJL, Marchetti E (2008) Thermal, seismic and infrasound observations of persistent explosive activity and conduit dynamics at Santiaguito lava dome. *Guatemala J Volcanol Geotherm Res* 173:1–14. doi:10.1016/j.jvolgeores.2007.11.026
- Scorer RS (1957) Experiments on convection of isolated masses of buoyant fluid. *J Fluid Mech* 2:583–594. doi:10.1017/S0022112057000397
- Spampinato L, Calvari S, Oppenheimer C, Boschi E (2011) Volcano surveillance using infrared cameras. *Earth-Sci Rev* 106:63–91. doi:10.1016/j.earscirev.2011.01.003
- Spampinato L, Oppenheimer C, Cannata A, Montalto P, Salerno GG, Calvari S (2012) On the time-scale of thermal cycles associated with open-vent degassing. *Bull Volcanol* 74:1281–1292. doi:10.1007/s00445-012-0592-2
- Spina L, Taddeucci J, Cannata A, Gresta S, Lodato L, Privitera E, Scarlato P, Gaeta M, Gaudin D, Palladino DM (2015) Explosive volcanic activity at Mt. Yasur: a characterization of the acoustic events (9–12th July 2011). *J Volcanol Geotherm Res* 302:24–32. doi:10.1016/j.jvolgeores.2015.07.027
- Sykes, J.B., 1982. *The concise Oxford dictionary of current English, based on the Oxford dictionary and its supplements.* Oxford University Press
- Tamburello G, Aiuppa A, Kantzas EP, McGonigle AJS, Ripepe M (2012) Passive vs. active degassing modes at an open-vent volcano (Stromboli, Italy). *Earth Planet Sci Lett* 359–360:106–116. doi:10.1016/j.epsl.2012.09.050
- Tamburello G, McGonigle AJS, Kantzas EP, Aiuppa A (2011) Recent advances in ground-based ultraviolet remote sensing of volcanic SO<sub>2</sub> fluxes. *Ann. Geophys* 54. doi:10.4401/ag-5179
- Tibaldi, A., Corazzato, C., Apuani, T., Pasquaré, F.A., Vezzoli, L., 2008. Geological-Structural Framework of Stromboli Volcano, Past Collapses, and the Possible Influence on the Events of the 2002–2003 Crisis, in: Calvari, S., Inguaggiato, S., Puglisi, G., Ripepe, M., Rosi, M. (Eds.). *The Stromboli Volcano: an integrated study of the 2002–2003 eruption.* American Geophysical Union, pp. 5–17
- Toramaru A (1989) Vesiculation process and bubble size distributions in ascending magmas with constant velocities. *J. Geophys. Res. Solid Earth* 94:17523–17542. doi:10.1029/JB094iB12p17523
- Turner, J.S., 1979. *Buoyancy effects in fluids.* Cambridge University Press
- Vergnolle S, Jaupart C (1986) Separated two-phase flow and basaltic eruptions. *J Geophys Res Solid Earth* 91:12842–12860. doi:10.1029/JB091iB12p12842
- Verhoeven JW (1996) Glossary of terms used in photochemistry (IUPAC recommendations 1996). *Pure Appl Chem* 68:2223–2286
- Washington HS (1917) Persistence of vents at Stromboli and its bearing on volcanic mechanism. *Geol Soc Am Bull* 28:249–278. doi:10.1130/GSAB-28-249